

pubs.acs.org/JPCL Letter

# Elucidation of Quantum-Well-Specific Carrier Mobilities in Layered Perovskites

Ninghao Zhou,<sup>†</sup> Zhenyu Ouyang,<sup>†</sup> Liang Yan, Meredith G. McNamee, Wei You, and Andrew M. Moran\*



Cite This: J. Phys. Chem. Lett. 2021, 12, 1116–1123



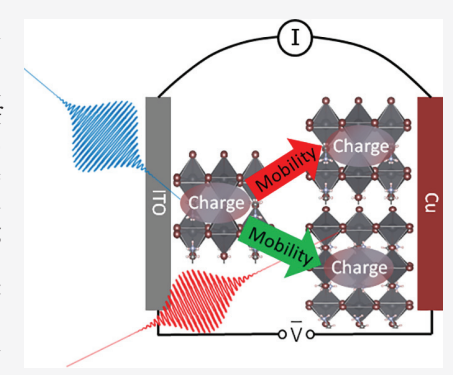
ACCESS

Metrics & More

Article Recommendations

supporting Information

ABSTRACT: Layered organohalide perovskite films consist of quantum wells with concentration distributions tailored to enhance long-range charge transport. Whereas cascaded energy and charge funneling behaviors have been detected with conventional optical spectroscopies, it is not clear that such dynamics contribute to the efficiencies of photovoltaic cells. In this Letter, we use nonlinear photocurrent spectroscopy to selectively target charge transport processes within devices based on layered perovskite quantum wells. The photocurrent induced by a pair of laser pulses is directly measured in this "action" spectroscopy to remove ambiguities in signal interpretation. By varying the external bias, we determine carrier mobilities for quantum-well-specific trajectories taken through the active layers of the devices. The results suggest that the largest quantum wells are primarily responsible for photocurrent production, whereas the smallest quantum wells trap charge carriers and are a major source of energy loss in photovoltaic cells.



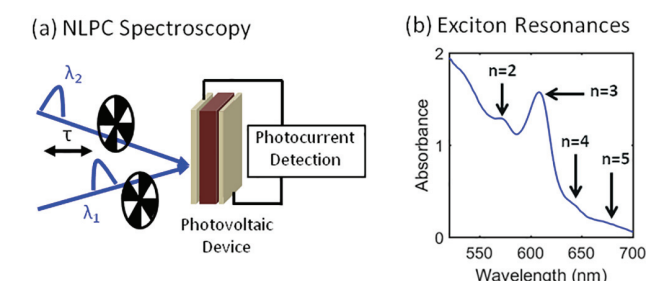
uantum wells with various sizes are organized to promote long-range energy and charge transport within layered organohalide perovskite materials. <sup>1–5</sup> In these systems, the thinnest and thickest quantum wells are most concentrated near opposing electrodes in photovoltaic cells, thereby establishing gradients in the average values of the band gaps and energy levels.<sup>5,6</sup> In this respect, the layered architectures are reminiscent of biological light-harvesting antennae (e.g., phycobilisome of cyanobacteria). For example, the layered perovskites investigated in our recent works are described by the general chemical formula  $BA_nMA_{n-1}Pb_nI_{3n+1}$ , where BA is butylammonium, MA is methylammonium, and the subscript *n* represents the number of stacked lead-iodide octahedra within the quantum wells. The band gaps, exciton resonance frequencies, and conduction band minima decrease as the thicknesses of the quantum wells increase (i.e., increase with n). Whereas the efficiencies of energy transfer processes are well characterized in these systems, the carrier funneling dynamics have not been fully established due to the absence of clear-cut spectroscopic signatures in conventional transient absorption experiments.  $^{8-15}$  The challenge in applying such purely optical techniques to layered perovskites is that the signals are dominated by excitons, which have large transition dipoles, rather than free charge carriers. 10,16 For this reason, the elucidation of carrier funneling processes in layered perovskites requires techniques capable of targeting charge transport on the nanosecond time scale of carrier drift through the active layer of a photovoltaic device.

We have recently demonstrated approaches for conducting two-dimensional "action" spectroscopies with applications to layered perovskite systems. 13,17,18 In this class of experiments, a sequence of laser pulses induces a spontaneous process whose nonlinear response is directly detected (e.g., fluorescence emission, photocurrent in a device, mass spectrometry). 19-33 Directly probing the action response of a material and/or device enhances physical insights by correlating elementary energy and charge transfer dynamics to the fates of the electronic excitations. As shown in Figure 1a, our experimental approach for nonlinear photocurrent spectroscopy (NLPC) resembles a conventional pump-probe method. The two narrowband (5 nm spectral widths) laser pulses are color tunable,  $\lambda_1$  and  $\lambda_2$ , and have an experimentally controlled delay time,  $\tau$ . This narrowband, color-tuning approach is appropriate for studies of layered perovskite systems because the nanosecond time scale of interest is much greater than the subpicosecond pulse durations. Moreover, the laser beams may be tuned into the resonances of specific quantum wells to characterize the trajectories taken by charge carriers through the active layer of a photovoltaic cell. For example, quantum wells in which n = 2, 3, 4, and 5 exhibit well-resolved exciton resonances near 570, 600, 640, and 680 nm, respectively.

Received: December 6, 2020 Accepted: January 12, 2021 Published: January 21, 2021









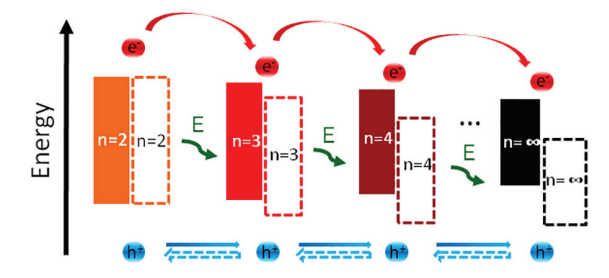


**Figure 1.** NLPC spectroscopy is used to determine quantum-well-specific carrier mobilities. (a) A pair of color tunable laser pulses with interpulse delay,  $\tau$ , is used to probe carrier transport within a photovoltaic device. (b) Exciton resonances for separate quantum wells are well resolved in the linear absorbance spectrum. (c) Band gaps of the quantum wells decrease as the index, n, increases. Electron and energy transfer are promoted toward the largest quantum wells. The direction of hole transport is determined by whether the system possesses a type I (shaded rectangles) or type II (open rectangles) band alignment.

In our recent application of NLPC spectroscopy to a layered perovskite system, we found evidence of a bottleneck associated with processes in which electrons transfer from the smaller (n = 2 and 3) to larger (n = 5) quantum wells, thereby calling into question the efficiency of the electron transfer cascade depicted in Figure 1c. The NLPC signal profiles indicated that electrons accumulate in domains occupied by the n = 2 and 3 quantum wells on the time scale of 3 ns; however, these measurements were unable to provide information regarding subsequent dynamics due to a limited delay range. Therefore, the implications of this apparent electron transfer cascade for the overall function of a photovoltaic device remain unclear. Access to the 10-20 ns time scale on which charge carriers fully traverse the active layer of a photovoltaic cell is required to draw firm conclusions regarding long-range carrier transport.

In this Letter, we apply an upgraded version of NLPC spectroscopy to layered perovskite-based photovoltaic cells to disentangle the quantum-well-specific trajectories taken by the charge carriers. First, in order to track carrier drift through the perovskite medium to the electron- and/or hole-selective layers of the photovoltaic cell, we have extended the delay range from 3 to 15 ns and fabricated devices with thinner active layers to reduce the carrier transit times. The full range of carrier transfer processes depicted in Figure 1c is now accessible with these improvements. Access to longer time and length scales will provide further insights into the efficiencies of cascaded pathways in which electrons transfer from the n=2 and 3 quantum wells to n=5 quantum wells. Second, we vary the external bias (and electric field, E) to establish drift velocities within the active layer,  $v_{\rm d}$ . The sum of electron and

hole mobilities,  $\mu$ , may then be determined with linear fits,  $\nu_{\rm d} = \mu E$ . Notably, the carrier mobilities determined in the present work are transport pathway specific in that the wavelengths of the two laser pulses,  $\lambda_1$  and  $\lambda_2$ , are tuned into the resonances of specific quantum wells. Such detailed knowledge of the carrier trajectories cannot be gathered by conventional methods of determining mobilities in which only one laser pulse is employed. <sup>34–39</sup>

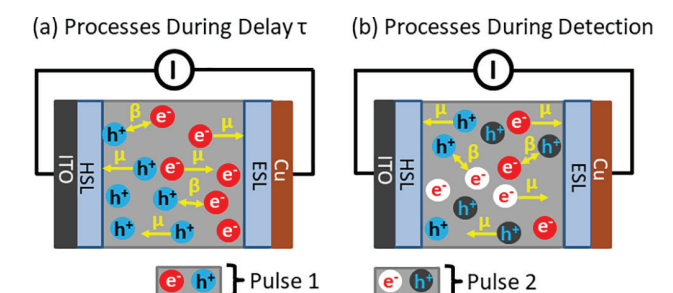
It is instructive to consider NLPC spectroscopy in the context of conventional time-of-flight methods (TOF) for determining mobilities within photovoltaic devices. 36-43 In this class of experiments, the photocurrent and/or fluorescence emission is monitored after photoexcitation to determine the transit time across the active layer of a device. Although a variety of processes may influence TOF decay profiles, carrier drift may be distinguished from other relaxation mechanisms by varying the external bias to isolate the component of the response that is sensitive to the applied electric field. 36,37 With inspiration from this earlier work, we suggest that NLPC signal generation mechanisms parallel those associated with conventional TOF techniques in many respects. For example, as shown in Figure 2, the first laser pulse employed in an NLPC experiment initiates carrier drift, two-body recombination, diffusion, and trapping in the delay time,  $\tau$ . Carrier drift and trapping compete to determine the amount of time required to clear photoexcited carriers from the active layer of a device. 41,42

In NLPC spectroscopy, the second laser pulse interacts with a small fraction of the carriers photoexcited by the first pulse. The probability that a carrier which was photoexcited by the first laser pulse will also interact with the second laser pulse can be calculated using the product of the absorbance cross section and laser fluence. With oscillator strengths ranging from 0.02 to 0.30 for quantum wells with various thicknesses, 16,44 we estimate that the absorbance cross sections are on the order of  $10^{-21}$ – $10^{-20}$  m<sup>2</sup>.<sup>45</sup> In addition, we have confirmed that an empirical cross section of approximately  $10^{-21} \ m^2$  is consistent with the ratio between linear and transient absorbance signals reported in ref 10. The probability that a carrier photoexcited by the first laser pulse will participate in the nonlinear response then ranges from  $10^{-5}$  to  $10^{-4}$  for a laser fluence of  $10^{16}$ photons/m<sup>2</sup>. Carriers photoexcited by either one of the two pulses (i.e., not both pulses) can recombine and drift while the signal is integrated; however, these carriers do not contribute to the signal because the nonlinear response is isolated by chopping the two laser beams (see Figure 1a).

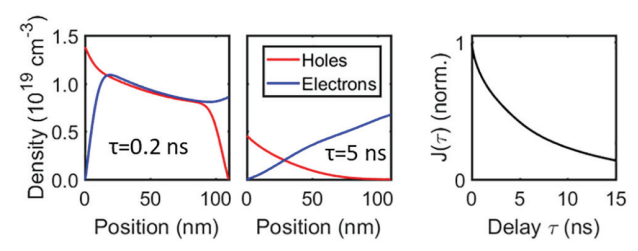
Further insight into the NLPC signal generation mechanisms may be gathered by combining long-range drift with perturbative response functions for a bulk semiconductor (see Supporting Information). We obtain the following expression for the magnitude of the ground state bleach (GSB)-like signal component at fourth order in time-dependent perturbation theory

$$S_{\text{GSB}}^{(4)}(\omega_1, \tau, \omega_2) = \sigma_{\text{abs}}(\omega_1)\sigma_{\text{abs}}(\omega_2) \int_0^\infty dt J(\tau, t)$$
 (1)

where  $\sigma_{\rm abs}(\omega)$  is the rate of absorbance (i.e., Fermi's golden rule) and the signal is obtained by integrating over the nonlinear response of the photocurrent,  $J(\tau,t)$ . The variable, t, represents the amount of time elapsed after the second laser pulse interacts with the active layer of a device. The magnitude of the excited-state emission-like nonlinearity can be simulated by replacing  $\sigma_{\rm abs}(\omega_2)$  with the emission rate  $\sigma_{\rm em}(\omega_2)$ 



(c) Calculations With Trap-Induced Velocity Dispersion



(d) Calculations Without Trap-Induced Velocity Dispersion

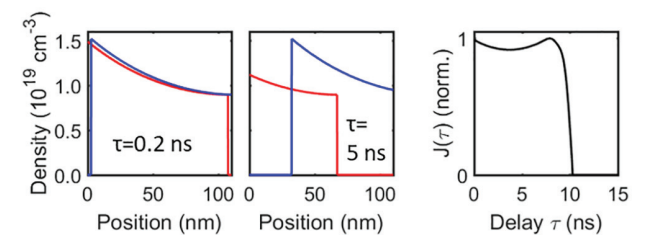


Figure 2. Summary of NLPC signal generation mechanisms. (a) Carrier drift  $(\mu)$ , two-body recombination  $(\beta)$ , and trapping govern dynamics in the delay time between laser pulses,  $\tau$ . HSL and ESL represent hole- and electron-selective layers. (b) Carriers photoexcited by the two laser pulses interact and drift while the signal is integrated. (c, d) Calculations show that trap-induced velocity dispersion inflates the overall transit time and induces a quasiexponential decay. Simulations conducted with and without carrier trapping yield decay profiles similar to those established for conventional TOF methods.

$$S_{\text{ESE}}^{(4)}(\omega_1, \tau, \omega_2) = \sigma_{\text{abs}}(\omega_1)\sigma_{\text{em}}(\omega_2) \int_0^\infty dt J(\tau, t)$$
 (2)

Similarly, an excited-state absorption-like term can be obtained by replacing  $\sigma_{\rm em}(\omega_2)$  with the rate of light absorption between singly and doubly excited states. Based on previous transient absorption microscopy results for these systems, our formulas are written under the assumption that the drift velocity is primarily governed by extrinsic properties of the material (e.g., traps, disorder, grain boundaries) rather than the natures of the quantum states.  $^{6,46,47}$ 

The delay-dependent electron and hole densities, which govern the nonlinear photocurrent  $J(\tau,t)$ , may be simulated with knowledge of the mobilities, two-body recombination coefficients, and trap-induced broadening of the carrier distributions (see Supporting Information). The two-body recombination coefficient of  $3.3 \times 10^{-9}$  cm<sup>3</sup>/s was obtained in earlier experimental work, 6,46 whereas we have set the mobility equal to 0.015 cm<sup>2</sup>/V/s based on the shapes of the NLPC decay curves observed in the experiments below. The charge carrier distributions plotted in Figure 2c show that two-body recombination reduces the carrier densities on a time scale

shorter than the transit time, thereby decreasing the overall magnitude of the photocurrent. Trap-induced velocity dispersion is accounted for by broadening of the distributions, which increases the effective transit time through the active layer. <sup>41,42</sup> In addition, the calculated NLPC signals demonstrate that carrier trapping promotes decay profiles with quasi-exponential shapes. These aspects of the NLPC signal generation mechanism are clarified by comparison to the signal calculated without carrier trapping (see Figure 2d). It is notable that the differences in the NLPC decay profiles closely resemble those observed in early conventional TOF studies. <sup>41</sup>

The procedure used in this work to determine carrier mobilities is outlined in Figure 3. NLPC decay curves are measured with wavelengths corresponding to the 16 points of intersections overlaid on the 2D NLPC spectra for layered and bulk perovskite-based devices (see Figures 3a and 3d). These four wavelengths correspond to the exciton resonances of the n=2, 3, 4, and 5 quantum wells, which are known to participate in relaxation processes for this layered system. The measurements are conducted at five different values of the external bias ranging from -0.2 to 0.2 V (three values of the bias are shown to reduce crowding in Figures 3b). Electric fields are computed by summing the external biases and the open circuit voltages then dividing by the thicknesses of the active layers. The average decay times are determined by fitting the NLPC decay profiles with the following equation:

$$S(\tau) = A_0 + A_1 \exp(-\tau/T_1) + A_2 \exp(-\tau/T_2)$$
 (3)

The average decay time,  $T_{\rm av}$ , is then computed by taking a weighted average of the time constants

$$T_{\rm av} = \frac{A_1 T_1}{A_1 + A_2} + \frac{A_2 T_2}{A_1 + A_2} \tag{4}$$

The drift velocity is given by the ratio of the active layer thickness and the average decay time,  $d/T_{\rm av}$ . Contributions to the decay profiles arising from diffusion, trapping, and the carrier lifetimes are removed by linear fitting because they are independent of (or depend weakly on) the applied electric field. For this reason, the intercept is subtracted from the data points in Figures 3c and 3f to isolate the drift velocity.

In Figures 3g and 3h, we compare NLPC profiles acquired for bulk and layered systems with  $\lambda_1 = 570$  nm and  $\lambda_2 = 680$ nm. The temporal profiles measured for the bulk system are sensitive to the external bias and decay monotonically. In contrast, the signals acquired for the layered system exhibit signatures of trapping in that the temporal profiles are independent of the external biases. The 3 ns rise in the signal magnitude is consistent with electron funneling from smaller (n = 2) to larger (n = 5) quantum wells (see Figure 1c), <sup>13</sup> whereas the subsequent decay represents a variety of relaxation processes. The region of the 2D spectrum above the diagonal is particularly sensitive to electron funneling because the laser pulses enter the device through the ITO substrate and must initially transmit through the region of the active layer in which the thinnest quantum wells are most concentrated. FIB milling measurements show that the n = 2 and n = 5 concentration profiles are poorly overlapped in this system;<sup>6</sup> however, the summary of mobilities presented below demonstrates that such ineffective carrier funneling processes generalize to other pairs of quantum wells.

In Figure 4, carrier mobilities determined at the 16 grid points of the 2D spectra are shown (see Figures 3a and 3d).

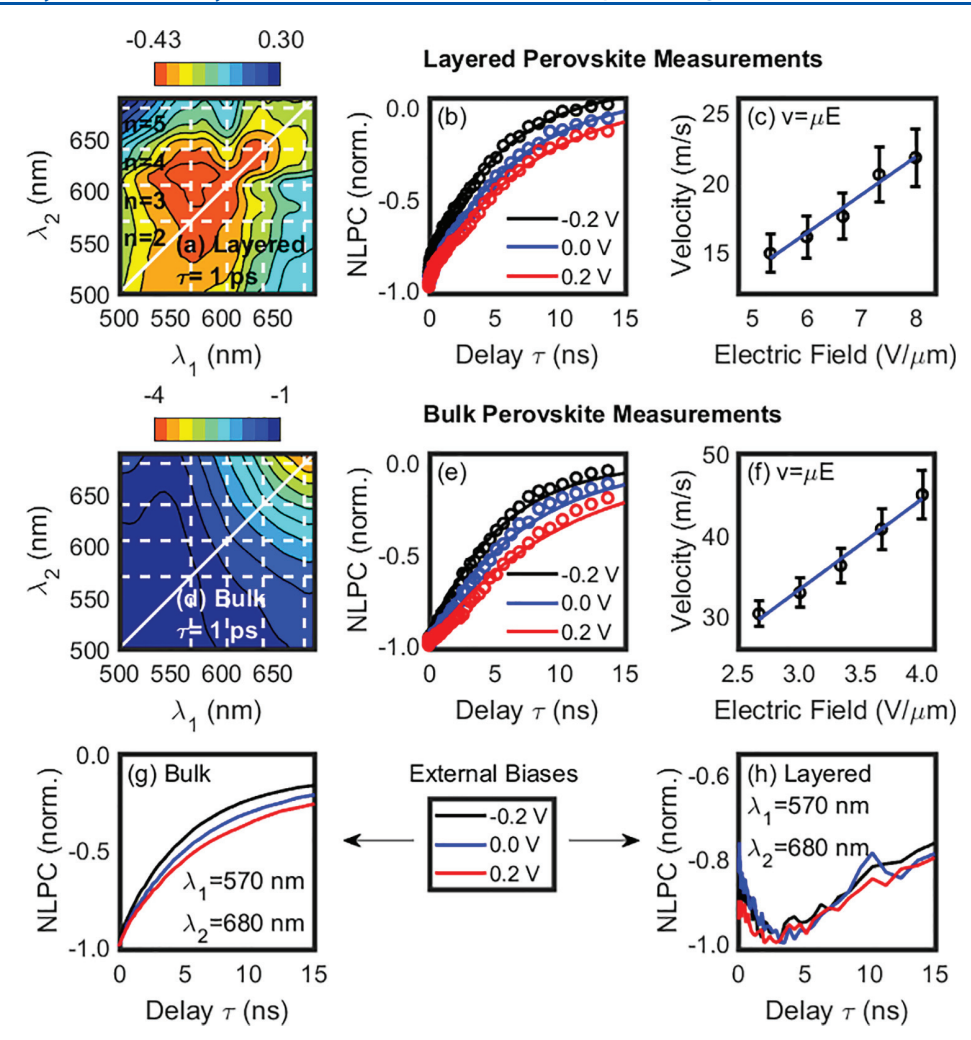


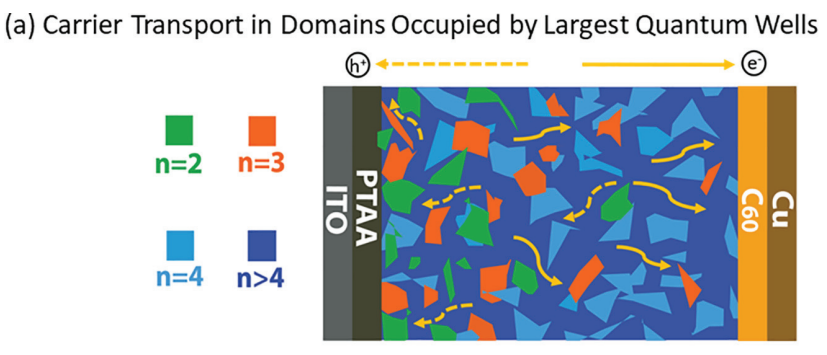
Figure 3. Determination of pathway-specific carrier mobilities for photovoltaic devices based on layered and bulk perovskites. Two-dimensional NLPC spectra are acquired for (a) layered and (d) bulk perovskite-based devices. Signals are plotted in units of microamperes ( $\mu$ A). (b, e) Temporal profiles are measured over a range of applied biases with  $\lambda_1 = \lambda_2 = 600$  nm. (c, f) Drift velocities are computed using the sample thicknesses and weighted averages of time constants. The slopes represent the carrier mobilities at specific values of  $\lambda_1$  and  $\lambda_2$ . Measurements conducted with  $\lambda_1 = 570$  nm and  $\lambda_2 = 680$  nm are compared for (g) bulk and (h) layered systems. Insensitivity to the external bias in the layered system is a signature of carrier trapping. The magnitudes of the signals are normalized to -1.0 for comparison of the decay profiles (the sign of the signal is negative because the photocurrent saturates as laser intensity increases).

The 2D mobility surface of the layered system exhibits a pronounced asymmetry above  $(\lambda_1 < \lambda_2)$  and below  $(\lambda_1 > \lambda_2)$ the diagonal of the spectrum. Above the diagonal, the mobilities correspond to the initiation of carrier transport in the smaller quantum wells (n = 2-3). For example, the cross peak between the n = 2 and 4 quantum wells is located at  $\lambda_1 =$ 570 nm and  $\lambda_2$  = 640 nm. In this region of the spectrum, we find that the drift velocities are insensitive to the external bias, which signifies carrier trapping in the domains occupied by the smallest quantum wells. 48 To our knowledge, carrier mobility measurements have not been reported for this particular film composition; however, the mobility determined using a conventional TOF method is 0.2 cm<sup>2</sup>/V/s for a system in which quantum well n = 4 has the greatest concentration.<sup>5</sup> In principle, a material dominated by n = 4 quantum wells should be more conductive than the film considered here, wherein the n = 3 systems have the greatest concentrations.

Figure 4b shows that the largest carrier mobilities are measured below the diagonal of the 2D NLPC spectrum for

the layered perovskite system. For example, the greatest carrier mobility, 0.036 cm<sup>2</sup>/V/s, is found with  $\lambda_1 = 680$  nm and  $\lambda_2 =$ 570 nm. This is not a signature of an extraordinary hole funneling mechanism (see Figure 1c). Rather, we suggest that both laser pulses interact with the n = 5 quantum well despite having different wavelengths because the optical response associated with this quantum well's continuum states spans the full visible wavelength range. 10,13 In this interpretation, the larger mobilities determined below the diagonal of the spectrum partly reflect the wavelength-dependent penetration depths of the incident light (see Supporting Information). That is, the 680 nm laser pulses transmit through the smaller quantum wells concentrated near the interface with the holeselective layer, thereby maximizing the initial concentrations of carriers in the thickest quantum wells. Quantum wells with larger values of n have the smallest exciton binding energies and most readily conduct charge carriers.<sup>50</sup>

The carrier mobilities determined for the bulk perovskite range from 0.016 to 0.026 cm<sup>2</sup>/V/s (see Figure 4c). In



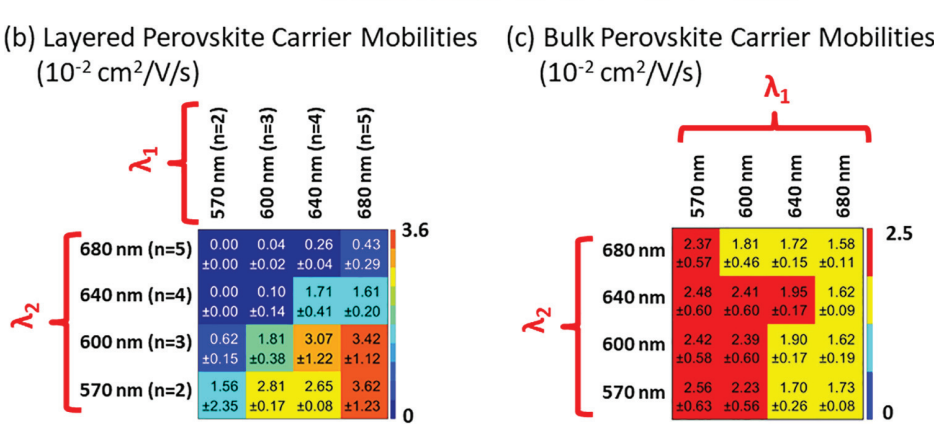


Figure 4. (a) NLPC measurements suggest that electron and hole transport occur in the phases of the thickest quantum wells in layered perovskite-based photovoltaic cells. Charge carrier funneling processes do not contribute to the photocurrent. (b) Quantum-well-specific carrier mobilities determined for layered perovskites reveal a pronounced asymmetry above and below the diagonal of the 2D mobility spectrum. The mobilities are smallest when the charge transport processes are initiated by photoexcitation of smaller quantum wells (n = 2-3). (c) Carrier mobilities determined for photovoltaic cells based on bulk perovskites depend weakly on the excitation wavelengths.

contrast to the layered system, the bulk mobilities exhibit a weak dependence on the excitation wavelengths and do not approach zero above the diagonal of the spectrum. We attribute the relatively flat mobility surface obtained for the bulk system to the homogeneous nature of the active layer. Carriers photoexcited at shorter wavelengths in the bulk perovskite cool and drift without transferring between separate phases of the material. Interestingly, our carrier mobilities are 50-100 times smaller than those determined using photoluminescence quenching data<sup>34,36</sup> but are in good agreement with the electron mobility obtained by measuring the steadystate space charge-limited current (0.012 cm<sup>2</sup>/V/s).<sup>49</sup> Contacts with the electrodes, interfaces with the transport layers, and space-charge effects can influence the mobilities measured with NLPC spectroscopy. Nonetheless, differences in the mobility surfaces presented in Figures 4b and 4c make clear the ability of the method to distinguish carrier trajectories in active layers possessing multiple components.

The present applications demonstrate the utility of NLPC spectroscopy for determining carrier mobilities in photovoltaic cells with heterogeneous active layers. Mobilities obtained using alternate methods provide less information regarding the specific trajectories taken by charge carriers through the active layer of a device. On the other hand, NLPC spectroscopy is challenged by a lack of precision in determining the carrier transit times, which originates in photoexcitation of the full thickness of the active layer (i.e., the active layer must be thin because the delay range is limited to 15 ns). For example, photoluminescence quenching experiments yield carrier mobilities by employing Einstein's relation between diffusion

and drift;<sup>51</sup> however, this method establishes only the initial conditions for transport with a single laser pulse.<sup>34,35</sup> In addition, terahertz spectroscopy, which is an important tool for establishing physical insights,<sup>52–54</sup> targets short-range motions and is relatively insensitive to "extrinsic" effects such as grain boundaries; terahertz methods conducted on perovskites have yielded carrier mobilities that are more than 10 times greater than those obtained with TOF and photoluminescence quenching techniques.<sup>38</sup>

In summary, our understanding of carrier transport within layered perovskite-based photovoltaic cells is summarized in Figure 4a. We suggest that charge carriers initiated in the thickest quantum wells traverse the active layer in a circuitous manner to avoid the debris of smaller quantum wells. The data indicate that the carrier funneling processes depicted in Figure 1c do not contribute to the production of photocurrent (i.e., carrier transport is not enhanced by favorable band alignments between quantum wells).<sup>55</sup> This conclusion is based on signatures of carrier trapping observed above the diagonal of the 2D NLPC spectrum, where the drift velocity is independent of the external bias (see Figure 4b). Below the diagonal, we find that carrier transport initiated in the thickest quantum wells gives rise to the greatest carrier mobilities. Whereas it has been shown that energy funneling influences the light-harvesting capability of a layered perovskite-based photovoltaic cell,<sup>5</sup> the present work suggests that such processes are far less efficient than direct photoexcitation and transport within a bulk perovskite-like phase of the active layer.

## **EXPERIMENTAL METHODS**

Synthesis and Device Fabrication. CH<sub>3</sub>(CH<sub>2</sub>)<sub>3</sub>NH<sub>3</sub>I (BAI) was synthesized from the reaction of *n*-butylamine in ethanol (1:1 by volume) with hydriodic acid (HI) (57 wt % in water without stabilizer) at 0 °C in an ice water bath. The crude product was obtained by slowly evaporating the solvent under reduced pressure at 60 °C for 1 h. The white powder was then recrystallized in ethanol and further washed with diethyl ether three times before drying it in a vacuum oven at 60 °C overnight. The powder was then transferred into a glovebox filled with nitrogen gas for future use. CH<sub>3</sub>NH<sub>3</sub>I (MAI) was synthesized by methylamine solution (40 wt % in H<sub>2</sub>O) with hydriodic acid (HI) (57 wt % in water without stabilizer) in a similar manner as BAI.

Glass substrates coated with patterned indium-doped tin oxide (ITO) were purchased from Thin Film Devices, Inc., with a sheet resistance of 20  $\Omega$ /square. Prior to use, the substrates were cleaned with an ultrasonic bath by deionized water, acetone, and 2-proponal for 15 min each in sequence. The substrates were dried under a stream of nitrogen gas and subjected to the treatment of UV—ozone for 15 min. Then, the substrates were transferred into the glovebox filled with nitrogen gas. PTAA (poly(triaryl amine) from Sigma-Aldrich) solution in toluene (2 mg/mL) was then spin-cast onto cleaned ITO substrates at 4000 rpm for 30 s and then baked at 100 °C for 10 min. After it was cooled to room temperature, perovskite precursor solution was spin-cast on the substrate with PTAA.

For BAI-based 2D perovskite solar cells with maximal concentrations of n=3 quantum wells, the precursor solution was made by dissolving BAI, MAI, and PbI<sub>2</sub> in DMF with the molar ratio of BAI/MAI/PbI<sub>2</sub> = 2:2:3, and the solution was stirred at 70 °C for 30 min. The concentration of Pb<sup>2+</sup> is 0.75 M to obtain about 200 nm and 0.5 M to obtain about 110 nm. The 2D perovskite film was obtained by spin-coating precursor solution at 70 °C on substrate (prewet by spin coating pure DMF on top at 2000 rpm for 3 s twice) at room temperature with 5000 rpm for 20 s in air. The resulting film was quickly transferred to a hot plate at 80 °C for 1 min.

For the 3D MAPbI<sub>3</sub> perovskite solar cell, the perovskite precursor solution was prepared by dissolving PbI2 and MAI in DMF/DMSO = 9:1. The concentration of  $Pb^{2+}$  is 1.0 M to obtain about 270 nm and 0.65 M to obtain about 140 nm. Then, MAPbI<sub>3</sub> precursor solution was spun onto PTAA (prewet by spin coating pure DMF on top at 2000 rpm for 3 s twice)-coated substrate at 2000 rpm for 2 s and at 4000 rpm for 20 s; the sample was drop-casted with 0.3 mL of toluene at 8 s of the second-step spin-coating. Subsequently, the sample was annealed at 65 °C for 10 min and 100 °C for 10 min. The spin coating process for 3D perovskite was done in a glovebox filled with nitrogen gas. After they were cooled, substrates with 2D and 3D perovskite film were transfer to another glovebox filled with nitrogen gas. Then, 40 nm C60, 3 nm BCP (Bathocuproine), and 80 nm copper were thermally evaporated at a base pressure of  $3 \times 10^{-7}$  Torr to finish the device. The active area was 0.13 cm<sup>2</sup> controlled by a shadow mask.

Device characterization was carried out under AM 1.5G irradiation with the intensity of 100 mW/cm<sup>2</sup> (Oriel 91160, 300 W) calibrated by a NREL certified standard silicon cell. Current density versus voltage (J-V) curves were recorded with a Keithley 2400 digital source meter. The scan rate is 0.05 V/s.

Nonlinear Photocurrent Spectroscopy. Nonlinear photocurrent experiments are conducted using an instrument described in previous works. <sup>10,13,17</sup> Briefly, all experiments are conducted with a 45 fs, 4 mJ Coherent Libra laser system. To begin, 1.5 mJ of the 800 nm fundamental is focused into a 2 m long tube filled with argon gas to generate a visible continuum. The continuum is split into two beams which pass through separate 4F spectral filters before arriving at the sample position. Color tunability is achieved by translating slits at the 2F planes of the filters

In this work, we have increased the delay range of the apparatus from 3 to 15 ns using a long-range, motorized translation stage (Zaber X-LDQ0600C-AE53D12). Four retroreflectors (Thorlabs) are mounted on the stage to maintain a small footprint. Collimation of the beam over this longer distance is achieved using a telescope with a +100 and  $-50~\rm mm$  singlet lenses. We have confirmed that transmission of the laser beam through a 100  $\mu \rm m$  pinhole at the sample position varies by less than 5% over the full range of parameters covered in these experiments.

Nonlinear photocurrent experiments are conducted using a pair of independently color-tunable laser beams, each with spectral widths of 5 nm. The laser pulses have 55 pJ energies and 82  $\mu$ m fwhm spot sizes. The laser fluence of 1.0  $\mu$ J/cm<sup>2</sup> is on the same order of magnitude as those employed in earlier NLPC-like experiments.<sup>24,27,28</sup> The photocurrent is amplified at either 2  $\mu$ A/V (layered perovskite) or 20  $\mu$ A/V (bulk perovskite) using a Stanford Research 570 current preamplifier. Signals are then processed with a National Instruments data acquisition board (NI USB-6221) that is synchronized to the laser system at 250 Hz (i.e., divide the laser's repetition rate by 4). The photocurrent is given by the product of the amplification factor and voltage recorded at the DAQ board. An adequate density of points is obtained by setting the sampling rate of the data acquisition board to 500 kHz. These parameters are chosen to maximize the dynamic range of the detection system. The two laser beams are chopped at 500 and 250 Hz, respectively. The signals are acquired under four conditions, i.e., pulse 1 only  $(S_1)$ , pulse 2 only  $(S_2)$ , pulses 1 and 2  $(S_{1+2})$ , and both pulses blocked  $(S_0)$ . The NLPC signal is defined as  $S_{\text{NLPC}} = S_{1+2} - S_1 - S_2 + S_0$ . Each photocurrent difference is averaged over a total of 800 laser shots (0.8 s).

Carrier mobilities are determined by measuring NLPC decay profiles at five external biases, i.e., -0.2, -0.1, 0, 0.1, and 0.2 V. The delay time,  $\tau$ , and wavelengths,  $\lambda_1$  and  $\lambda_2$ , are also scanned in these experiments. We cycle through the full set of conditions 30 times to produce a single data set with a total data acquisition time of 24 h. To establish reproducibility, the experiments are repeated at least three times with separate devices. These data are also consistent with NLPC measurements reported for the same quantum well composition. The standard deviations reported in Figure 4 correspond to these repeated measurements (i.e., not to fitting parameters for a single experiment). The individual data sets, which are used to compute the averaged mobilities in Figure 4, are presented in the Supporting Information.

## ASSOCIATED CONTENT

## Supporting Information

The Supporting Information is available free of charge at https://pubs.acs.org/doi/10.1021/acs.jpclett.0c03596.

Discussion of light penetration depths in the layered system, a model for NLPC spectroscopy, scanning electron microscopy images, full data sets obtained for separate photovoltaic devices, and the instrument response function (PDF)

## AUTHOR INFORMATION

## **Corresponding Author**

Andrew M. Moran — Department of Chemistry, University of North Carolina at Chapel Hill, Chapel Hill, North Carolina 27599, United States; oorcid.org/0000-0001-7761-7613; Email: ammoran@email.unc.edu

#### Authors

Ninghao Zhou — Department of Chemistry, University of North Carolina at Chapel Hill, Chapel Hill, North Carolina 27599, United States; orcid.org/0000-0002-7255-282X

Zhenyu Ouyang — Department of Chemistry, University of North Carolina at Chapel Hill, Chapel Hill, North Carolina 27599, United States; orcid.org/0000-0001-9549-0353

Liang Yan — Department of Chemistry, University of North Carolina at Chapel Hill, Chapel Hill, North Carolina 27599, United States; © orcid.org/0000-0003-4122-7466

Meredith G. McNamee – Department of Chemistry, University of North Carolina at Chapel Hill, Chapel Hill, North Carolina 27599, United States; orcid.org/0000-0003-4432-5870

Wei You − Department of Chemistry, University of North Carolina at Chapel Hill, Chapel Hill, North Carolina 27599, United States; ⊙ orcid.org/0000-0003-0354-1948

Complete contact information is available at: https://pubs.acs.org/10.1021/acs.jpclett.0c03596

## **Author Contributions**

These authors contributed equally.

### Notes

The authors declare no competing financial interest.

# **■** ACKNOWLEDGMENTS

This work is supported by the National Science Foundation under CHE-1763207 (N.Z., Z.O., M.M., and A.M.). L.Y. and W.Y. acknowledge the support from the UNC Research Opportunities Initiative (ROI) through the Center of Hybrid Materials Enabled Electronic Technology. Research of 2D perovskites fabrication was supported by the Center for Hybrid Organic Inorganic Semiconductors for Energy (CHOISE), an Energy Frontier Research Center funded by the U.S. Department of Energy (DOE), Office of Science, Office of Basic Energy Sciences (BES). SEM images were obtained at the Chapel Hill Analytical and Nanofabrication Laboratory, CHANL, a member of the North Carolina Research Triangle Nanotechnology Network, RTNN, which is supported by the National Science Foundation, grant ECCS-2025064, as part of the National Nanotechnology Coordinated Infrastructure, NNCI.

## REFERENCES

- (1) Cao, D. H.; Stoumpos, C. C.; Farha, O. K.; Hupp, J. T.; Kanatzidis, M. G. 2D Homologous Perovskites as Light-Absorbing Materials for Solar Cell Applications. *J. Am. Chem. Soc.* **2015**, *137*, 7843–7850.
- (2) Yuan, M.; Quan, L. N.; Comin, R.; Walters, G.; Sabatini, R.; Voznyy, O.; Hoogland, S.; Zhao, Y.; Beauregard, E. M.; Kanjanaboos,

- P.; Lu, Z.; Kim, D. H.; Sargent, E. H. Perovskite Energy Funnels for Efficient Light-Emitting Diodes. *Nat. Nanotechnol.* **2016**, *11*, 872–877.
- (3) Stoumpos, C. C.; Cao, D. H.; Clark, D. J.; Young, J.; Rondinelli, J. M.; Jang, J. I.; Hupp, J. T.; Kanatzidis, M. G. Ruddlesden—Popper Hybrid Lead Iodide Perovskite 2D Homologous Semiconductors. *Chem. Mater.* **2016**, 28, 2852—2867.
- (4) Mauck, C. M.; Tisdale, W. A. Excitons in 2D Organic–Inorganic Halide Perovskites. *Trends Chem.* **2019**, *1*, 380–393.
- (5) Lin, Y.; Fang, Y.; Zhao, J.; Shao, Y.; Stuard, S. J.; Nahid, M. M.; Ade, H.; Wang, Q.; Shield, J. E.; Zhou, N.; Moran, A. M.; Huang, J. Unveiling the Operation Mechanism of Layered Perovskite Solar Cells. *Nat. Commun.* **2019**, *10*, 1008.
- (6) Williams, O. F.; Zhou, N.; Hu, J.; Ouyang, Z.; Kumbhar, A.; You, W.; Moran, A. M. Imaging Excited State Dynamics in Layered 2D Perovskites with Transient Absorption Microscopy. *J. Phys. Chem. A* **2019**, *123*, 11012–11021.
- (7) MacColl, R.; Guard-Friar, D. *Phycobilisomes*; CRC Press: Boca Raton, 1987.
- (8) Liu, J.; Leng, J.; Wu, K.; Zhang, J.; Jin, S. Observation of Internal Photoinduced Electron and Hole Separation in Hybrid Two-Dimensional Perovskite Films. *J. Am. Chem. Soc.* **2017**, *139*, 1432–1435.
- (9) Shang, Q.; Wang, Y.; Zhong, Y.; Mi, Y.; Qin, L.; Zhao, Y.; Qiu, X.; Liu, X.; Zhang, Q. Unveiling Structurally Engineered Carrier Dynamics in Hybrid Quasi-Two-Dimensional Perovskite Thin Films Toward Controllable Emission. *J. Phys. Chem. Lett.* **2017**, *8*, 4431–4438
- (10) Williams, O. F.; Guo, Z.; Hu, J.; Yan, L.; You, W.; Moran, A. M. Energy Transfer Mechanisms in Layered 2D Perovskites. *J. Chem. Phys.* **2018**, *148*, 134706.
- (11) Yan, L.; Hu, J.; Guo, Z.; Chen, H.; Toney, M. F.; Moran, A. M.; You, W. General Post-Annealing Method Enables High-Efficiency Two-Dimensional Perovskite Solar Cells. *ACS Appl. Mater. Interfaces* **2018**, *10*, 33187–33197.
- (12) Proppe, A. H.; Elkins, M. H.; Voznyy, O.; Pensack, R. D.; Zapata, F.; Besteiro, L. V.; Quan, L. N.; Quintero-Bermudez, R.; Todorovic, P.; Kelley, S. O.; Govorov, A. O.; Gray, S. K.; Infante, I.; Sargent, E. H.; Scholes, G. D. Spectrally Resolved Ultrafast Exciton Transfer in Mixed Perovskite Quantum Wells. *J. Phys. Chem. Lett.* **2019**, *10*, 419–426.
- (13) Zhou, N.; Ouyang, Z.; Hu, J.; Williams, O. F.; Yan, L.; You, W.; Moran, A. M. Distinguishing Energy- and Charge-Transfer Processes in Layered Perovskite Quantum Wells with Two-Dimensional Action Spectroscopies. *J. Phys. Chem. Lett.* **2020**, *11*, 4570–4577.
- (14) Cho, J.; DuBose, J. T.; Kamat, P. V. Charge Carrier Recombination Dynamics of Two-Dimensional Lead Halide Perovskites. J. Phys. Chem. Lett. 2020, 11, 2570–2576.
- (15) Lin, D.; Ma, L.; Ni, W.; Wang, C.; Zhang, F.; Dong, H.; Gurzadyan, G. G.; Nie, Z. Unveiling Hot Carrier Relaxation and Carrier Transport Mechanisms in Quasi-Two-Dimensional Layered Perovskites. J. Mater. Chem. A 2020, 8, 25402—25410.
- (16) Hong, X.; Ishihara, T.; Nurmikko, A. V. Dielectric Confinement Effect on Excitons in PbI<sub>4</sub>-Based Layered Semiconductors. *Phys. Rev. B: Condens. Matter Mater. Phys.* **1992**, 45, 6961–6964.
- (17) Zhou, N.; Hu, J.; Ouyang, Z.; Williams, O. F.; Yan, L.; You, W.; Moran, A. M. Nonlinear Photocurrent Spectroscopy of Layered 2D Perovskite Quantum Wells. J. Phys. Chem. Lett. 2019, 10, 7362–7367.
- (18) Ouyang, Z.; Zhou, N.; Hu, J.; Williams, O. F.; Yan, L.; You, W.; Moran, A. M. Nonlinear fluorescence spectroscopy of layered perovskite quantum wells. *J. Chem. Phys.* **2020**, *153*, 134202.
- (19) Lanzani, G.; Zenz, C.; Cerullo, G.; Graupner, W.; Leising, G.; Scherf, U.; De Silvestri, S. Femtosecond Photovoltage Excitation Cross-Correlation on a Ladder-Type Polymer. *Synth. Met.* **2000**, 111–112, 493–496.
- (20) Müller, J. G.; Scherf, U.; Lemmer, U. Two Step Charge Carrier Generation in a Ladder-Type Conjugated Polymer. *Synth. Met.* **2001**, *119* (1), 395–396.

- (21) Tian, P.; Keusters, D.; Suzaki, Y.; Warren, W. S. Femtosecond Phase-Coherent Two-Dimensional Spectroscopy. *Science* **2003**, *300*, 1553–1555.
- (22) Tekavec, P. F.; Lott, G. A.; Marcus, A. H. Fluorescence-Detected Two-Dimensional Electronic Coherence Spectroscopy by Acousto-Optic Phase Modulation. *J. Chem. Phys.* **2007**, *127*, 214307.
- (23) Bakulin, A. A.; Rao, A.; Pavelyev, V. G.; van Loosdrecht, P. H. M.; Pshenichnikov, M. S.; Niedzialek, D.; Cornil, J.; Beljonne, D.; Friend, R. H. The Role of Driving Energy and Delocalized States for Charge Separation in Organic Semiconductors. *Science* **2012**, 335 (6074), 1340.
- (24) Nardin, G.; Autry, T. M.; Silverman, K. L.; Cundiff, S. T. Multidimensional Coherent Photocurrent Spectroscopy of a Semi-conductor Nanostructure. *Opt. Express* **2013**, *21*, 28617–28627.
- (25) Karki, K. J.; Widom, J. R.; Seibt, J.; Moody, I.; Lonergan, M. C.; Pullerits, T.; Marcus, A. H. Coherent Two-Dimensional Photocurrent Spectroscopy in a PbS Quantum Dot Photocell. *Nat. Commun.* **2014**, *5*, 5869.
- (26) Vella, E.; Li, H.; Grégoire, P.; Tuladhar, S. M.; Vezie, M. S.; Few, S.; Bazán, C. M.; Nelson, J.; Silva-Acuña, C.; Bittner, E. R. Ultrafast Decoherence Dynamics Govern Photocarrier Generation Efficiencies in Polymer Solar Cells. *Sci. Rep.* **2016**, *6*, 29437.
- (27) Bakulin, A. A.; Silva, C.; Vella, E. Ultrafast Spectroscopy with Photocurrent Detection: Watching Excitonic Optoelectronic Systems at Work. *J. Phys. Chem. Lett.* **2016**, *7*, 250–258.
- (28) Grégoire, P.; Srimath Kandada, A. R.; Vella, E.; Tao, C.; Leonelli, R.; Silva, C. Incoherent Population Mixing Contributions to Phase-Modulation Two-Dimensional Coherent Excitation Spectra. *J. Chem. Phys.* **2017**, *147*, 114201.
- (29) Tiwari, V.; Matutes, Y. A.; Gardiner, A. T.; Jansen, T. L. C.; Cogdell, R. J.; Ogilvie, J. P. Spatially-Resolved Fluorescence-Detected Two-Dimensional Electronic Spectroscopy Probes Varying Excitonic Structure in Photosynthetic Bacteria. *Nat. Commun.* **2018**, *9*, 4219.
- (30) Malý, P.; Mančal, T. Signatures of Exciton Delocalization and Exciton—Exciton Annihilation in Fluorescence-Detected Two-Dimensional Coherent Spectroscopy. *J. Phys. Chem. Lett.* **2018**, *9*, 5654–5659
- (31) Mueller, S.; Draeger, S.; Ma, X.; Hensen, M.; Kenneweg, T.; Pfeiffer, W.; Brixner, T. Fluorescence-Detected Two-Quantum and One-Quantum-Two-Quantum 2D Electronic Spectroscopy. *J. Phys. Chem. Lett.* **2018**, *9*, 1964–1969.
- (32) Roeding, S.; Brixner, T. Coherent Two-Dimensional Electronic Mass Spectrometry. *Nat. Commun.* **2018**, *9*, 2519.
- (33) Whaley-Mayda, L.; Penwell, S. B.; Tokmakoff, A. Fluorescence-Encoded Infrared Spectroscopy: Ultrafast Vibrational Spectroscopy on Small Ensembles of Molecules in Solution. *J. Phys. Chem. Lett.* **2019**, *10*, 1967–1972.
- (34) Xing, G.; Mathews, N.; Sun, S.; Lim, S. S.; Lam, Y. M.; Grätzel, M.; Mhaisalkar, S.; Sum, T. C. Long-Range Balanced Electron- and Hole-Transport Lengths in Organic-Inorganic CH<sub>3</sub>NH<sub>3</sub>PbI<sub>3</sub>. *Science* **2013**, 342, 344–347.
- (35) Stranks, S. D.; Eperon, G. E.; Grancini, G.; Menelaou, C.; Alcocer, M. J.; Leijtens, T.; Herz, L. M.; Petrozza, A.; Snaith, H. J. Electron-Hole Diffusion Lengths Exceeding 1 Micrometer in an Organometal Trihalide Perovskite Absorber. *Science* **2013**, 342, 341–344
- (36) Dong, Q.; Fang, Y.; Shao, Y.; Mulligan, P.; Qiu, J.; Cao, L.; Huang, J. Electron-Hole Diffusion Lengths > 175 μm in Solution-Grown CH3NH3PbI3 Single Crystals. *Science* **2015**, 347, 967–970.
- (37) Shi, D.; Adinolfi, V.; Comin, R.; Yuan, M.; Alarousu, E.; Buin, A.; Chen, Y.; Hoogland, S.; Rothenberger, A.; Katsiev, K.; Losovyj, Y.; Zhang, X.; Dowben, P. A.; Mohammed, O. F.; Sargent, E. H.; Bakr, O. M. Low Trap-State Density and Long Carrier Diffusion in Organolead Trihalide Perovskite Single Crystals. *Science* 2015, 347, 519–522.
- (38) Herz, L. M. Charge-Carrier Mobilities in Metal Halide Perovskites: Fundamental Mechanisms and Limits. ACS Energy Lett. **2017**, 2, 1539–1548.
- (39) Peng, J.; Chen, Y.; Zheng, K.; Pullerits, T.; Liang, Z. Insights Into Charge Carrier Dynamics in Organo-Metal Halide Perovskites:

- From Neat Films to Solar Cells. Chem. Soc. Rev. 2017, 46, 5714-5729.
- (40) Schwartz, L. M.; Hornig, J. F. Photocurrents Generated by Intense Flash Illumination. *J. Phys. Chem. Solids* **1965**, 26, 1821–1824
- (41) Spear, W. E. Drift Mobility Techniques for the Study of Electrical Transport Properties in Insulating Solids. *J. Non-Cryst. Solids* **1969**, *1*, 197.
- (42) Karl, N., Charge-Carrier Mobility in Organic Crystals. In Organic Electronic Materials Conjugated Polymers and Low Molecular Weight Organic Solids, Farchoni, R.; Grosso, G., Eds.; Springer-Verlag: New York, 2001.
- (43) Cusumano, P.; Gambino, S. Space Charge and Carrier Trapping Effects on the Transient Photocurrents of Organic Materials Using the Time-of-Flight Technique. *J. Electron. Mater.* **2008**, 37, 231–239.
- (44) Ishihara, T. Optical Properties of PbI-Based Perovskite Structures. *J. Lumin.* **1994**, *60-61*, 269–274.
- (45) Hilborn, R. C. Einstein Coefficients, Cross sections, f Values, Dipole Moments, and All That. Am. J. Phys. 1982, 50, 982–986.
- (46) Guo, Z.; Zhou, N.; Williams, O. F.; Hu, J.; You, W.; Moran, A. M. Imaging Carrier Diffusion in Perovskites with a Diffractive Optic-Based Transient Absorption Microscope. *J. Phys. Chem. C* **2018**, *122*, 10650–10656.
- (47) Hickey, C. L.; Grumstrup, E. M. Direct Correlation of Charge Carrier Transport to Local Crystal Quality in Lead Halide Perovskites. *Nano Lett.* **2020**, *20*, 5050–5056.
- (48) Wu, X.; Trinh, M. T.; Niesner, D.; Zhu, H.; Norman, Z.; Owen, J. S.; Yaffe, O.; Kudisch, B. J.; Zhu, X.-Y. Trap States in Lead Iodide Perovskites. J. Am. Chem. Soc. 2015, 137, 2089–2096.
- (49) Sajedi Alvar, M.; Blom, P. W. M.; Wetzelaer, G.-J. A. H. Space-Charge-Limited Electron and Hole Currents in Hybrid Organic-Inorganic Perovskites. *Nat. Commun.* **2020**, *11*, 4023.
- (50) Blancon, J.-C.; Stier, A. V.; Tsai, H.; Nie, W.; Stoumpos, C. C.; Traoré, B.; Pedesseau, L.; Kepenekian, M.; Katsutani, F.; Noe, G. T.; Kono, J.; Tretiak, S.; Crooker, S. A.; Katan, C.; Kanatzidis, M. G.; Crochet, J. J.; Even, J.; Mohite, A. D. Scaling Law for Excitons in 2D Perovskite Quantum Wells. *Nat. Commun.* **2018**, *9*, 2254.
- (51) Kubo, R. The Fluctuation-Dissipation Theorem. Rep. Prog. Phys. 1966, 29, 255-284.
- (52) Ponseca, C. S.; Savenije, T. J.; Abdellah, M.; Zheng, K.; Yartsev, A.; Pascher, T.; Harlang, T.; Chabera, P.; Pullerits, T.; Stepanov, A.; Wolf, J.-P.; Sundström, V. Organometal Halide Perovskite Solar Cell Materials Rationalized: Ultrafast Charge Generation, High and Microsecond-Long Balanced Mobilities, and Slow Recombination. *J. Am. Chem. Soc.* **2014**, *136*, 5189.
- (53) Milot, R. L.; Eperon, G. E.; Snaith, H. J.; Johnston, M. B.; Herz, L. M. Temperature-Dependent Charge-Carrier Dynamics in CH3NH3Pbl3 Perovskite Thin Films. *Adv. Funct. Mater.* **2015**, *25*, 6218–6227.
- (54) Li, C.; Yang, J.; Su, F.; Tan, J.; Luo, Y.; Ye, S. Conformational disorder of organic cations tunes the charge carrier mobility in two-dimensional organic-inorganic perovskites. *Nat. Commun.* **2020**, *11*, 5481
- (55) Zhang, L.; Zhang, X.; Lu, G. Band Alignment in Two-Dimensional Halide Perovskite Heterostructures: Type I or Type II? *J. Phys. Chem. Lett.* **2020**, *11*, 2910–2916.